Physics-Based Quadratic Deformation Using Elastic Weighting

Ran Luo [ID], Weiwei Xu, *Member, IEEE*, Huamin Wang, *Member, IEEE*,
Kun Zhou [ID], *Fellow, IEEE*, and Yin Yang [ID], *Member, IEEE*

Abstract—This paper presents a *spatial reduction* framework for simulating nonlinear deformable objects interactively. This reduced model is built using a small number of overlapping quadratic domains as we notice that incorporating high-order degrees of freedom (DOFs) is important for the simulation quality. Departing from existing multi-domain methods in graphics, our method interprets deformed shapes as blended quadratic transformations from nearby domains. Doing so avoids expensive safeguards against the domain coupling and improves the numerical robustness under large deformations. We present an algorithm that efficiently computes weight functions for reduced DOFs in a physics-aware manner. Inspired by the well-known multi-weight enveloping technique, our framework also allows subspace tweaking based on a few representative deformation poses. Such elastic weighting mechanism significantly extends the expressivity of the reduced model with light-weight computational efforts. Our simulator is versatile and can be well interfaced with many existing techniques. It also supports local DOF adaption to incorporate novel deformations (i.e., induced by the collision). The proposed algorithm complements state-of-the-art model reduction and domain decomposition methods by seeking for good trade-offs among animation quality, numerical robustness, pre-computation complexity, and simulation efficiency from an alternative perspective.

Index Terms—Quadratic deformation, FEM, model reduction, domain decomposition, weight function

✦

1 INTRODUCTION

REALISTICALLY simulating nonlinear deformable objects is known to be expensive, which drives a great amount of research efforts for developing accelerating techniques. An intuitive thought is to leverage the fact that deformations in reality are often of low rank, as elastic material models themselves effectively penalize high-frequency shape variations. Speedups of orders of magnitude can be obtained by removing less important degrees of freedom (DOFs). The core question for such *model reduction* method is how to utilize limited DOFs to achieve a better deformation expressivity. This objective is often dealt with either *spectrally* or *spatially*.

Spectral subspace methods assign each DOF with a global representative modal shape or *mode*, often obtained using PCA or modal analysis [3], [4]. They rely on a dedicated pre-computation to select key modes. Some recent research further accelerates the pre-computation [5], [6] nevertheless, it is still at the order of $O(rN^2)$, where r stands

for the number of modes and N is the size of the input model. It is also known that a globally constructed modal subspace lacks the capability of capturing local deformations. To remedy this limitation, the domain decomposition method (DDM) trends to be a more attractive option. It allows a domain-level mode customization and makes the local pre-computation much more efficient (i.e., $O(rN^2/d)$ for d domains, which is parallelizable and re-usable if domains are of the same geometry). When domains are *non-overlapping*, the influence of domain's subspace is analogous to the nodal *shape function* in the finite element method (FEM), which evaluates 1 locally and 0 elsewhere. As an unpleasant consequence, domains need to be explicitly coupled due to such boundary discontinuity. This gives rise to another concern regarding the simulation robustness under large deformations. Highly deformed domain interfaces could fail most coupling methods adopted in existing nonlinear multi-domain simulators like rigid binding [1], damped springs [7], or coupling elements [2].

Another collection of acceleration techniques, referred to as *spatial reduction* here, scatters DOFs sparsely over the deformable body and utilizes blending functions to express the deformation in between, similar to the Cage-based [8] or the Free-from [9] schemes widely used for shape modeling. Here, the concept of DOF is not limited to the nodal displacement. It could be a linear transformation field [10], a local coordinate frame [11], or an integration unit [12]. The adopted blend or *weight functions* smoothly mix deformations across domains and unnecessitate an explicit domain coupling. As a result, the spatial reduction behaves more stably against extreme deformations. This framework is also better suited for local adaptivity and refinement [13],
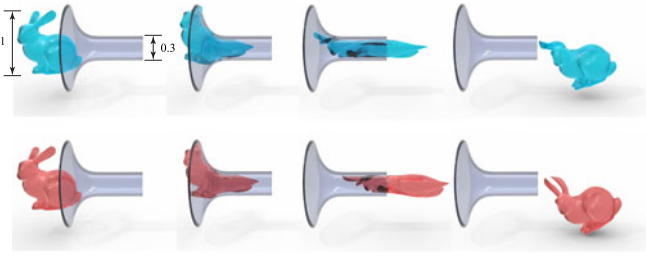
Fig. 1. Overlapping quadratic domains make the simulation robust even under large deformations. The one-inch-tall bunny model is forced to pass a funnel whose inner diameter is only 0.3 inch. Our method yields plausible animations (the red bunny) at an interactive rate comparable to the fullspace simulation (the blue bunny). Most existing non-overlapping multi-domain simulators (i.e., [1], [2]) fail in this challenging test. Indeed, our simulator remains stable even when the funnel's diameter is reduced to 0.2 inch (Fig. 16). Please refer to the supplementary video and executables for more details.

	Single-domain spectral reduction	Multi-domain spectral reduction	Spatial reduction	Our method
Fast pre-computation	🚫	✓	✓	✓
Good nonlinear expressivity	✓	✓	🚫	✓
Robust under large deformation	✓	🚫	✓	✓
Good local adaptivity	🚫	🚫	✓	✓

Fig. 2. Pros and cons of existing single- and multi-domain reduction techniques for nonlinear deformable models.

[14] than the spectral method. On the downside, since weight functions are typically calculated geometrically, they do not accommodate real material parameters like the Young's modulus and the Poisson's ratio. The deviation of the resulting deformation from the fullspace standard is often visually noticeable.

As outlined in Fig. 2, our method supplements state-of-the-art spatial reduction techniques and tries to provide better answers to following three important how-tos:

- How to choose suitable deformation DOFs?
- How to assign limited DOFs in a more profitable way?
- How to design a good weight function?

We show that it is *essential*, for nonlinear models, to employ high-order DOFs in the spatial reduction, and we build our reduced simulator using overlapping quadratic domains so that it remains stable even under extreme-scale deformations. Orthogonal to existing geometric weighting methods, we propose a new physics-based strategy yielding local, smooth and material-respecting weight functions. We borrow the idea of multi-weight enveloping (MWE) for animation skinning [15] and fine-tune weight functions based on a few given representative deformations. Experiments (i.e., an example is given in Fig. 1) show that such augmentation enhances the expressivity of the reduced model significantly even with few input poses. This elastic weighting mechanism is efficient and adaptable so that adding new quadratic DOFs at the simulation runtime is possible.

2 RELATED WORK

Physics-based deformable model has been extensively studied in computer graphics. We refer readers to excellent review articles [16], [17] for a comprehensive overview of classic deformable simulation algorithms. Speeding up a deformable simulation can be achieved using dedicated numerical treatments like the multigrid method [18], [19], an incremental matrix update [20], or parallelizable nonlinear solvers [21], [22]. These methods focus on improving the performance for the fullspace nonlinear optimization without condensing simulation DOFs. On the other hand, spectral reduction methods remove less important DOFs and create a reduced or subspace representation of fullspace DOFs (i.e., $\mathbf{u} = \mathbf{Uq}$). Modal analysis [3], [23], [24] and its

first-order modal derivatives [4] are often considered as the most effective way for the spectral subspace construction. Yang and colleagues [6] used Krylov iteration with reduced orthogonalization to further speed up this calculation. Displacement vectors from recent fullspace simulations can also be utilized as subspace bases [25].

Earlier spectral reduction techniques compute $\mathbf{U}$ globally, which become a bit awkward when localized deformations are desired unless the user includes a large number of modal bases. As a response to this limitation, domain decomposition methods, originally designed for large-scale numerical partial differential equations (PDEs), have been imported to graphics. As subspaces are constructed at domains, local deformations can be better handled. Many existing multi-domain solvers are non-overlapping. Consequently – domains must be explicitly constrained at boundaries, which stands as a primary challenge for state-of-the-art multi-domain deformable models. Roughly speaking, domain coupling can be achieved either geometrically [1], [26] by enforcing the shape continuity at the interface, or physically [2], [7] by plugging in coupling forces between adjacent domains. Recently, overlapping domain decomposition has also been explored in graphics. Xu and Barbič [27] used bounded bi-harmonics weights (BBW) to blend local modal derivative bases for localized deformations. While targeting on character skinning, it implies that overlapping domain decomposition is a feasible solution for local deformation effects. Following this direction, our method can also be considered as an overlapping domain decomposition system. Unlike [27], which geometrically blends physically-computed subspace bases, our method physically blends geometrically-constructed bases.

Alternatives are also possible for local deformations. For instance, Harmon and Zorin [28] made the fast simulation of contact-trigger deformations possible by adding local modal subspaces based on the Boussinesq solution. However, this method becomes less powerful when handling other types of local deformations. Teng and colleagues [29] extended the linear condensation to handle unpredicted deformations by evoking the fullspace simulation locally.

Our algorithm falls into another category of spatial reduction methods. Inspired by the superior accuracy of the higher-order finite element method [30], [31], we choose to build our deformable model based on overlapping quadratic domains, and each domain can be considered as a generalized *super element*. Our method also shares similar spirits of the shape match method [32]. Unlike shape matching however, our dynamics formulation is fully physics-based.
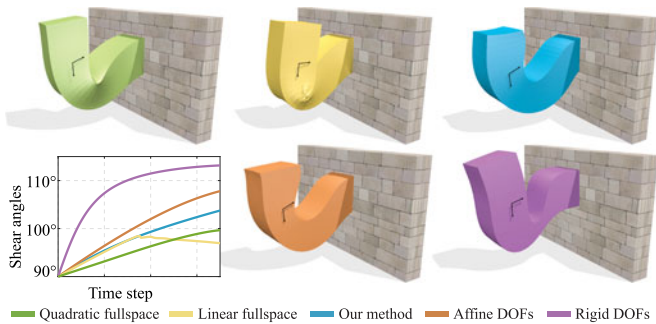
Fig. 3. We apply pure bending moments along the neutral axis of the beam model. The bending quality is measured using the maximum shearing angle along the neutral axis. Our method yields a much smaller shearing locking artifact than other competitors including affine DOFs [10], and rigid DOFs [11]. The ground truth is the result using full-space quadratic tetrahedral elements. Under such challenging bending test, even fullspace simulation using linear elements will fail.

Material parameters are fully incorporated in our reduced representation. This is achieved by encoding physically calculated shape functions, which is referred to as *elastic weighting* in this article. Calculating weight functions for shape interpolation has been widely studied in computer animation (see e.g., [33]). The harmonic coordinate [34], radial basis function (RBF) [35] and mean value coordinate (MVC) [36], [37] are a few classic paradigms. Similar techniques are also used in meshless simulations: Martin and colleagues [12] used the generalized moving least square (GMLS) for local deformation gradient evaluation. Gilles and colleagues [11] used harmonic kernels to blend rigid body motions for a skinning-like simulation.

We are not the first trying to accommodate material-awareness in the weight function calculation. Faure and colleagues [10] built shape functions using stiffness-scaled distance or the *compliance distance*. However, the other important material parameter of Poisson's ratio is disregarded. Nesme and colleagues [38] used static analysis to compute the weight function, which is similar to our approach. Yet, it is not clear how boundary conditions should be imposed. Meanwhile, it is difficult to rely on a single weight function to describe complex nonlinear deformations across the deformable body. Consequently, we calculate supplementary differential weight functions for quadratic DOFs based on few given representative deformation poses. This approach is similar to the multi-weight enveloping [15], [39].

3   QUADRATIC DOFS

Before starting a detailed discussion of our overlapping multi-domain simulator, we first show that quadratic DOFs are important in spatial reduction. Illustrated as the inset, think of simulating a simple 2D square
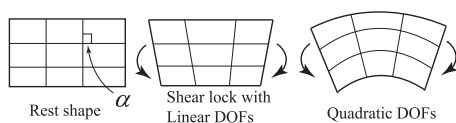

under the *pure bending* using quadrilateral elements. Because only bending moments are applied, the angle α should be unchanged and retain right during the bending. Unfortunately, if the local subspace (i.e., shape functions of the quad-element) is linear, straight lines stay straight, and

an artificial shear stress will be produced because α cannot be a right angle. More importantly, the shearing energy often increases one- or even two-order (depends on the element's geometry) faster than the real bending energy, which stiffens the deformable body. This artifact is known as the *shear locking* of linear elements. Shear locking is suppressed when the elements arrangement is dense as in most FEM based graphics simulations. However when simulation DOFs are spatially sparse (i.e., in our case), the locking issue becomes much more severe if we only have affine/linear [10] or rigid [11] DOFs.

To further illustrate this issue, we show an extreme example with side-by-side comparisons among several popular choices for local DOFs in Fig. 3. The beam model undergoes a pure bending test, where external forces applied are always perpendicular to its neutral axis. The force magnitude linearly varies along the neutral axis (as

shown on the left). Under this circumstance, the deformable object will only have nonlinear bending deformation. This simulation is particularly challenging for linear elements. As shown in the figure, even with the correction of the invertible finite element (IFE) method [40], the fullspace simulation using linear tetrahedral elements still fails this test. While quadratic 10-node tetrahedral elements produce a convincing ground truth result (with the cost of a much slower simulation). We evaluate the bending quality by examining the shearing angle as marked in the figure. A single quadratic domain (30 DOFs) captures the bending better than three affine domains [10] (36 DOFs) and five rigid domains [11] (30 DOFs).
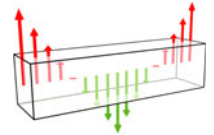
4   DEFORMABLE QUADRATIC MODEL

We design our reduced model using overlapping quadratic domains. Each domain houses 30 DOFs grouped into 3 translation DOFs, 9 affine DOFs, 9 quadratic homogenous DOFs, as well as 9 quadratic heterogenous DOFs. The kinematics of an individual domain is the same as in [12]. A domain only influences a local region, and the global deformation is obtained by combining contributions from multiple nearby domains.

Kinematics. For a given material point P on the deformable body, we denote $\mathbf{x} = [x_1, x_2, x_3]^\top$ and $\mathbf{u} = [u_1, u_2, u_3]^\top$ as its rest shape position and displacement. A nearby domain imposes a quadratic influence to its displacement components such that $u_i = \mathbf{x}^\top \mathbf{Q}_i \mathbf{x} + \mathbf{a}_i^\top \mathbf{x} + t_i$ for $i = 1, 2, 3$. $\mathbf{Q}_i \in \mathbb{R}^{3\times3}$ is a symmetric tensor encoding the iso-quadratic DOFs. We put its three diagonal DOFs into a vector $\mathbf{q}_{o_i} = [Q_{11}, Q_{22}, Q_{33}]^\top$ and name it as *homogenous* DOFs. Similarly, the vector $\mathbf{q}_{e_i} = [2Q_{12}, 2Q_{23}, 2Q_{13}]^\top$ containing off-diagonal entries of $\mathbf{Q}_i$ is referred to as *heterogenous* DOFs. The *affine* DOF $\mathbf{a} \in \mathbb{R}^3$ describes how u_i is linearly related to its rest position, and t_i is a *translation* DOF. Each type of deformable DOFs from different domains are convexly combined, and the ith displacement component of P can be written as

$$u_i = \sum_j w^j \left(t_i^j + \mathbf{a}_i^{j\top} \mathbf{x} + \mathbf{q}_{o_i}^{j\top} \widetilde{\mathbf{x}} + \mathbf{q}_{e_i}^{j\top} \widehat{\mathbf{x}} \right), \qquad (1)$$

where w^j is the location-dependent weight coefficient indicating how much domain j affects the displacement of P. $\widetilde{\mathbf{x}} = [x_1^2, x_2^2, x_3^2]^\top$ and $\widehat{\mathbf{x}} = [x_1 x_2, x_2 x_3, x_1 x_3]^\top$ are second-order homogenous and heterogenous vectors of P. By stacking all the DOFs from the jth domain into a single vector $\mathbf{q}^j \in \mathbb{R}^{30}$ such that $\mathbf{q}^j = [\mathbf{t}^{j\top}, \mathbf{a}_1^{j\top}, \mathbf{a}_2^{j\top}, \mathbf{a}_3^{j\top}, \mathbf{q}_{o_1}^{j\top}, \mathbf{q}_{o_2}^{j\top}, \mathbf{q}_{o_3}^{j\top}, \mathbf{q}_{e_1}^{j\top}, \mathbf{q}_{e_2}^{j\top}, \mathbf{q}_{e_3}^{j\top}]^\top$, the displacement of P can be concisely expressed as a matrix-vector product

$$\mathbf{u} = \mathbf{G}^j \mathbf{q}^j = \left[\mathbf{G}_t^j | \mathbf{G}_a^j | \mathbf{G}_o^j | \mathbf{G}_e^j \right] \mathbf{q}^j, \qquad (2)$$

where

$$\mathbf{G}_t^j = w^j \mathbf{I}, \quad \mathbf{G}_a^j = w^j \mathbf{I} \otimes \mathbf{x}^\top, \quad \mathbf{G}_o^j = w^j \mathbf{I} \otimes \widetilde{\mathbf{x}}^\top, \quad \mathbf{G}_e^j = w^j \mathbf{I} \otimes \widehat{\mathbf{x}}^\top.$$

We call matrix $\mathbf{G}^j$ the *geometric displacement matrix*, and the generalized coordinate $\mathbf{q}^j$ prescribes P's kinematic configuration as:

$$\dot{\mathbf{u}} = \sum_j \mathbf{G}^j \dot{\mathbf{q}}^j, \qquad \ddot{\mathbf{u}} = \sum_j \mathbf{G}^j \ddot{\mathbf{q}}^j. \qquad (3)$$

Reduced dynamics. Let $\mathbf{e}_i$ denote canonical basis vectors of $\mathbb{R}^3$, and we drop the domain superscript $[\cdot]^j$ for succincter notations. Based on Eq. (1), each row of the deformation gradient tensor $\mathbf{F} = [\mathbf{F}_1, \mathbf{F}_2, \mathbf{F}_3]^\top \in \mathbb{R}^{3 \times 3}$ can be written as $\mathbf{F}_i = \mathbf{F}_{t_i} + \mathbf{F}_{a_i} + \mathbf{F}_{o_i} + \mathbf{F}_{e_i} + \mathbf{e}_i$, where

$$\mathbf{F}_{t_i} = \sum \nabla w t_i, \qquad \mathbf{F}_{a_i} = \sum \mathbf{a}_i^\top \mathbf{x} \nabla w + w \mathbf{a}_i^\top,$$
$$\mathbf{F}_{o_i} = \sum \mathbf{q}_{o_i}^\top \widetilde{\mathbf{x}} \nabla w + w \mathbf{q}_{o_i}^\top \widetilde{\mathbf{X}}, \qquad \mathbf{F}_{e_i} = \sum \mathbf{q}_{e_i}^\top \widehat{\mathbf{x}} \nabla w + w \mathbf{q}_{e_i}^\top \widehat{\mathbf{X}},$$

and

$$\widetilde{\mathbf{X}} = \begin{bmatrix} x_2 & x_1 & 0 \\ 0 & x_3 & x_2 \\ x_3 & 0 & x_1 \end{bmatrix}, \qquad \widehat{\mathbf{X}} = \begin{bmatrix} 2x_1 & 0 & 0 \\ 0 & 2x_2 & 0 \\ 0 & 0 & 2x_3 \end{bmatrix}.$$

Here we assume that ∇w is a column 3-vector. On the top of $\mathbf{F}$, one can evaluate the nonlinear Green strain, $\mathbf{E} = \frac{1}{2}(\mathbf{F}^\top \mathbf{F} - \mathbf{I})$, and proceed to express the strain energy density Ψ as well as the first Piola-Kirchhoff stress tensor (PK1) based on the chosen material model. Our framework works with most hyperelastic materials, and in this paper we choose to use the St. Venant-Kirchhoff (StVK) model since it is capable of producing most desired deformation effects for computer animation. With the StVK model, the energy density and PK1 are formulated as: $\Psi = \mu \mathbf{E} : \mathbf{E} + \frac{\lambda}{2} \text{tr}^2(\mathbf{E})$ and $\mathbf{P} = \mathbf{F}[2\mu \mathbf{E} + \lambda \text{tr}(\mathbf{E})\mathbf{I}]$ respectively, where λ and μ are the Lamé parameters. The per-domain reduced internal force $\widetilde{\mathbf{f}}_{int}$ and its gradient $\partial \widetilde{\mathbf{f}}_{int} / \partial \mathbf{q}$ are computed as

$$\widetilde{\mathbf{f}}_{int} = - \int \mathbf{P} : \frac{\partial \mathbf{F}}{\partial \mathbf{q}} dV, \qquad (4)$$

and

$$\frac{\partial \widetilde{\mathbf{f}}_{int}}{\partial \mathbf{q}} = - \int \left(\frac{\partial \mathbf{P}}{\partial \mathbf{F}} : \frac{\partial \mathbf{F}}{\partial \mathbf{q}} \right)^\top : \frac{\partial \mathbf{F}}{\partial \mathbf{q}} dV. \qquad (5)$$

Here, $\partial \mathbf{F} / \partial \mathbf{q} \in \mathbb{R}^{3 \times 3 \times 30}$ is a block-sparse 3-tensor, which can be understood as the superposition of three layers as shown on the right. The ith layer represents the matrix $\partial \mathbf{F}_i / \partial \mathbf{q}$ and it hosts four sub-matrices: $\partial \mathbf{F}_{t_i} / \partial \mathbf{t}$, $\partial \mathbf{F}_{a_i} / \partial \mathbf{a}$, $\partial \mathbf{F}_{o_i} / \partial \mathbf{q}_o$
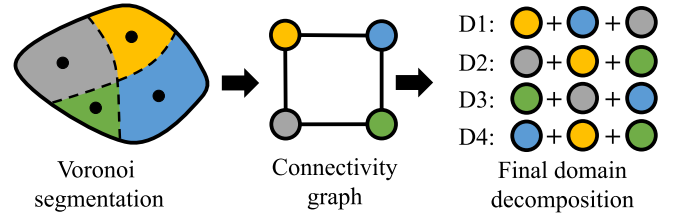

Fig. 4. Decompose a deformable body into four domains.

and $\partial \mathbf{F}_{e_i} / \partial \mathbf{a}_e$. These sub-matrices are block-sparse as the partial derivative is nonzero only when subscripts of generalized coordinates agree with each other. Each nonzero block can be easily calculated as

$$\frac{\partial \mathbf{F}_{t_i}}{\partial t_i} = \nabla w, \qquad \frac{\partial \mathbf{F}_{a_i}}{\partial \mathbf{a}_i} = \nabla w \otimes \mathbf{x} + w\mathbf{I},$$
$$\frac{\partial \mathbf{F}_{o_i}}{\partial \mathbf{q}_{o_i}} = \nabla w \otimes \widetilde{\mathbf{x}} + w\widetilde{\mathbf{X}}^\top, \quad \frac{\partial \mathbf{F}_{e_i}}{\partial \mathbf{q}_{e_i}} = \nabla w \otimes \widehat{\mathbf{x}} + w\widehat{\mathbf{X}}^\top. \qquad (6)$$

Applying temporal discretization using the implicit Euler integration leads to the final nonlinear system to be solved at each time step:

$$\left(\widetilde{\mathbf{M}} - h\widetilde{\mathbf{C}} - h^2 \frac{\partial \widetilde{\mathbf{f}}_{int}}{\partial \mathbf{q}} \right) \Delta \dot{\mathbf{q}} = h\widetilde{\mathbf{f}}_{ext} + h^2 \frac{\partial \widetilde{\mathbf{f}}_{int}}{\partial \mathbf{q}} \dot{\mathbf{q}}, \qquad (7)$$

where $\widetilde{\mathbf{M}}$ is the reduced mass matrix, which can be evaluated block-wisely: $\widetilde{\mathbf{M}}^{ij} = \int \rho \mathbf{G}^{i\top} \mathbf{G}^j dV$; $\widetilde{\mathbf{f}}_{ext}$ is the generalized external force; h is the time step size; and $\widetilde{\mathbf{C}}$ is the reduced damping matrix.

5 PHYSICS-BASED ELASTIC WEIGHTING

Analogous to FEM shape functions that blend nodal quantities volumetrically within an element, the weight function $w(\mathbf{x})$ interpolates local quadratic transformations to produce the final global result. An ideal weighting mechanism should be *material-customized* so that sparsely allocated DOFs well capture the nonlinear dynamics. To this end, we utilize the per-domain static equilibrium to retrieve the most physically meaningful weight distribution with carefully prescribed boundary conditions. It may be difficult to depict complex deformations with a single weight function. To address this challenge, we use a method similar to the multi-weight enveloping [15] to customize weight distributions for quadratic DOFs using an alternating optimization. The block-sparse matrix brought by decomposed domains allows a block-Jacobi solver to update weight coefficients efficiently.

Domain decomposition. The input tetrahedral mesh is decomposed into overlapping domains. As illustrated in Fig. 4, the domain decomposition starts with subdividing the mesh into non-overlapping *segments* as in [10], [11]. While many well-established mesh segmentation algorithms are available [41], we found that a centroid Voronoi tessellation typically suffices. Initial seeds of each Voronoi cell are obtained by a regular sampling within the bounding box of the input model, followed by a few Lloyd iterations [42]. Users are allowed to manually specify segments with the

Fig. 5. The Voronoi segmentation and corresponding domain decomposition of the bunny model.

provided interface too. After that, we can extract an undirected graph $\mathcal{G}(\mathcal{V}, \mathcal{E})$ encoding the connectivity information of the resulting Voronoi segmentation such that each vertex $v_i \in \mathcal{V}$ on the graph represents a Voronoi cell and $\langle v_i, v_j \rangle \in \mathcal{E}$ iff v_i and v_j share at least a triangle face. Finally, a domain is defined as a set of face-connected tetrahedrons from the ones in v_i and v_i's adjacent segments, and its seed is the seed of v_i. Note that it is possible that domains have the same collection of elements. For instance in Fig. 5 the red and purple, and the blue and green domains coincide with each other entirely, but they have complimentary weight functions.

Principal direction. The weight function of a domain ought to comply with the pattern describing how the deformation amplitude dissipates from its seed, where the maximum local displacement occurs. Following this thought, a reasonable way is to solve a static equilibrium [10], [38], by imposing an external nodal force $\mathbf{f}_s$ at the seed while retaining other neighbor seeds and domain's boundary. Unfortunately, this solution is ill-defined as we have infinite numbers of choices for applying $\mathbf{f}_s$ – obviously they lead to different weight distributions especially when the domain's geometry and material are irregular.

We resolve this ambiguity by restricting $\mathbf{f}_s$ along the *principal direction* $\mathbf{p}$. It can be understood as the *most deformable direction* such that domain's displacement is maximized when $\mathbf{f}_s = \mathbf{p}$. Let $[\cdot]_s$ and $[\cdot]_n$ denote domain's (three) seed DOFs and non-seed DOFs.[1] We partition domain's stiffness matrix accordingly and the principal direction of the domain can be mathematically formulated as a quadratically constrained quadratic program (QCQP) problem

$$\underset{\mathbf{p}}{\arg\max} \quad \|\mathbf{u}\|$$

$$\text{subject to} \quad \underbrace{\begin{bmatrix} \mathbf{K}_{ss} & \mathbf{K}_{sn} & \mathbf{0} \\ \mathbf{K}_{sn}^\top & \mathbf{K}_{nn} & \mathbf{C}^\top \\ \mathbf{0} & \mathbf{C} & \mathbf{0} \end{bmatrix}}_{\mathbf{K}} \begin{bmatrix} \mathbf{u}_s \\ \mathbf{u}_n \\ \lambda \end{bmatrix} = \begin{bmatrix} \mathbf{p} \\ \mathbf{0}_n \\ \mathbf{0}_\lambda \end{bmatrix}, \quad (8)$$

$$\text{and} \quad \|\mathbf{p}\| = 1.$$

Here λ is the unknown multiplier vector. $\mathbf{C}$ is a constraint matrix prescribing necessary boundary conditions, which include: 1) user specified constraints like anchor nodes; 2) seeds of neighbor Voronoi cells; and 3) domain's boundary DOFs (as shown on the right). Doing so makes the resulting weight function always evaluate 1 at its own seed and 0 at others'. It is also local and has a

Boundary cond. for ⬤+🟡+🟢
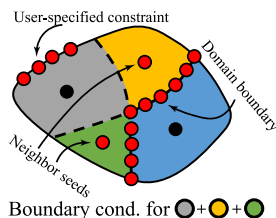
1. Seed DOFs are the x, y, and z displacement freedoms of the domain's seed node while non-seed DOFs are the DOFs of the non-seed nodes.

vanished influence outside the domain. $\mathbf{K}$ is the domain's stiffness matrix (using linear elements).

In general, QCQP is NP-hard [43]. However as Eq. (8) only activates low-dimensional equality constraints, it can be efficiently solved. To do so, we first rewrite the linear constraint term in Eq. (8) using partitioned *compliance matrix* $\mathbf{L}$ (i.e., $\mathbf{L} \triangleq \mathbf{K}^{-1}$) as

$$\begin{bmatrix} \mathbf{u}_s \\ \mathbf{u}_n \\ \lambda \end{bmatrix} = \begin{bmatrix} \mathbf{L}_{ss} & \mathbf{L}_{sn} & \mathbf{L}_{s\lambda} \\ \mathbf{L}_{sn}^\top & \mathbf{L}_{nn} & \mathbf{L}_{n\lambda} \\ \mathbf{L}_{s\lambda}^\top & \mathbf{L}_{n\lambda}^\top & \mathbf{L}_{\lambda\lambda} \end{bmatrix} \begin{bmatrix} \mathbf{p} \\ \mathbf{0}_n \\ \mathbf{0}_\lambda \end{bmatrix},$$

which leads to

$$\mathbf{u} = \begin{bmatrix} \mathbf{u}_s \\ \mathbf{u}_n \end{bmatrix} = \begin{bmatrix} \mathbf{L}_{ss} \\ \mathbf{L}_{sn}^\top \end{bmatrix} \mathbf{p} \triangleq \widetilde{\mathbf{L}} \mathbf{p}. \quad (9)$$

While evaluating the full $\mathbf{L}$ matrix is expensive, $\widetilde{\mathbf{L}}$ only has three columns and it can be quickly computed by solving

$$\mathbf{K} \begin{bmatrix} \mathbf{L}_{ss} \\ \mathbf{L}_{sn}^\top \\ \mathbf{L}_{s\lambda}^\top \end{bmatrix} = \begin{bmatrix} \mathbf{I}_s \\ \mathbf{0}_n \\ \mathbf{0}_\lambda \end{bmatrix}. \quad (10)$$

Recalling that $\mathbf{KL} = \mathbf{I}$, it is easy to understand that the right hand side of Eq. (10) is simply the first three column of the identity matrix. After that, the target function to be maximized becomes:

$$\|\mathbf{u}\| = \sqrt{\mathbf{p}^\top \mathbf{B} \mathbf{p}}, \qquad \mathbf{B} = \widetilde{\mathbf{L}}^\top \widetilde{\mathbf{L}}. \quad (11)$$

$\mathbf{B}$ is a symmetric positive definite (SPD) matrix and can be diagonalized with the eigenvalue decomposition as: $\mathbf{B} = \mathbf{R}^\top \Sigma \mathbf{R}$, where $\Sigma = \mathtt{diag}(d_1, d_2, d_3)$, $d_1 \leq d_2 \leq d_3$ is the diagonal matrix of eigenvalues. $\mathbf{R}$ is an orthonormal matrix. Substituting $\mathbf{B}$ by $\mathbf{R}^\top \Sigma \mathbf{R}$ in Eq. (11) yields

$$\|\mathbf{u}\| = \sqrt{(\mathbf{Rp})^\top \mathtt{diag}(d_1, d_2, d_3)(\mathbf{Rp})} \leq \sqrt{d_3}. \quad (12)$$

It shows that $\|\mathbf{u}\|$ reaches the maximum value $\sqrt{d_3}$ when $\mathbf{p}$ is the eigenvector of $\mathbf{B}$ corresponding to its largest eigenvalue.

Principal weight & principle projection. After $\mathbf{p}$ is ready, one can solve domain's static equilibrium prescribing $\mathbf{p}$ as the seed displacement and use the norm of the corresponding nodal displacement as its weight coefficient. Unfortunately, the resulting weight distribution leads to noticeable locking artifacts. Reasons are twofold. First, using the displacement norm as weight coefficients rules out the possibility of negative weight values, which are essential for high-order overlapping shape/weight functions. Second, when nodes are completely fixed, weight distributions among them are damped (as shown in Fig. 6a) making the corresponding region artificially stiffened. The solution is simple: since the principal direction reveals the most deformable direction of the domain, we should only consider the displacement along it other than incorporating information from "less important" directions.

Following this rationale, we allow all the constrained nodes to move on a plane perpendicular to the principal direction and only restrict their displacements along $\mathbf{p}$. The resulting per-node equilibrium displacement is also projected on $\mathbf{p}$ as the final *principal weight*. As illustrated in
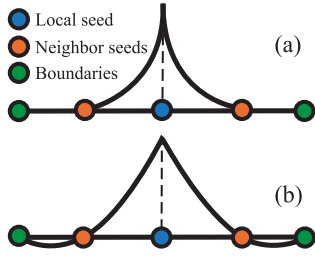
Fig. 6. (a) Anchoring boundary nodes completely results in weight damping. (b) Principal projection yields smoother weight functions.
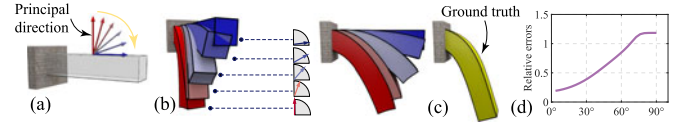

Fig. 7. Computing weight function along different directions other than the principal direction leads to locking artifacts. (a) shows the rest shape of the beam, whose principal direction is along the y axis. We show its equilibrium shapes under the gravity using weight functions calculated with directions further and further away from the principal direction. The resulting shapes are aggregated for the comparison. The ground truth is also given in (c). In (d) we plot the relative shape difference for different directions.

Fig. 6b, such principal projection is able to produce a natural and smooth weight distribution with necessary negative values across the domain. Clearly, the principal direction plays an essential role forming the principal weight function. Since different deformations propagate over the domain with different patterns, the principal direction effectively captures the most dominant one. Thus, animations produced using the principal weight are often distinguishably better. A simple test shown in Fig. 7 validates the importance of principal direction. In this test, the beam model only has one domain seeded at the middle. The principal direction is vertical to its neutral axis. We compare its deformation using weight functions calculated under a direction that is gradually away from the principal one (from $0°$ to $90°$ as shown in the figure). It can be clearly seen that the more it diverges from the principal direction, the more locking artifacts are observed.

Elastic weighting encodes both domain's material and geometry information. Our experiment shows that the principal weight yields more realistic animations compared with geometry-based weights (e.g., harmonic coordinate [34], RBF [35] or MVC [36], [37]) especially when the material of the deformable body is heterogeneous (e.g., see Section 7, Fig. 12).

Elastic multi-weight enveloping. While the principal weight function captures most visible deformations and produces natural results in general, the expressivity of our reduced model can be further enriched by using more customized weight functions at high-order DOFs, given a few representative shapes. Our method is similar to the multi-weight enveloping method [15], and we name this approach as elastic multi-weight enveloping (EMWE). Since the Cubature scheme [44] is also used for a fast runtime integration. Such shapes can be picked out of the Cubature training pose set if not specially provided.

We split domain's geometric displacement matrix $\mathbf{G}$ (i.e., Eq. (2)) into two sub-matrices $\mathbf{G} = [\mathbf{Y}|\mathbf{Z}]$ defined as $\mathbf{Y} = [\mathbf{G}_t|\mathbf{G}_a]$ and $\mathbf{Z} = [\mathbf{G}_o|\mathbf{G}_e]$ housing the linear and quadratic parts of $\mathbf{G}$ matrix respectively. Similarly, we subdivide domain's reduced coordinate into $\mathbf{y} = [\mathbf{t}^\top, \mathbf{a}_1^\top, \mathbf{a}_2^\top, \mathbf{a}_3^\top]^\top$ and $\mathbf{z} = [\mathbf{q}_{o_1}^\top, \mathbf{q}_{o_2}^\top, \mathbf{q}_{o_3}^\top, \mathbf{q}_{e_1}^\top, \mathbf{q}_{e_2}^\top, \mathbf{q}_{e_3}^\top]^\top$ so that $\mathbf{u} = \mathbf{Gq} = \mathbf{Yy} + \mathbf{Zz}$.

$\mathbf{Y}$ matrix is constructed using the principal weight function discussed previously. For a given exemplar shape $\mathbf{u}_k$, we compute its residual error vector as

$$\Delta\mathbf{u}_k \triangleq \left(\mathbf{I} - \mathbf{Y}(\mathbf{Y}^\top\mathbf{Y})^{-1}\mathbf{Y}^\top\right)\mathbf{u}_k, \qquad (13)$$

which is a difference vector between the shape $\mathbf{u}_k$ and its best-fitting reduced representation in the column space of $\mathbf{Y}$ (i.e., $(\mathbf{YY}^\top)^{-1}\mathbf{Y}^\top\mathbf{u}_k$). Our goal is to minimize $\|\Delta\mathbf{u}_k - \mathbf{Zz}\|$ by assigning each quadratic DOF an independent isotropic

weight function so that $\mathbf{u}_k$ can be well expressed in the subspace. Mathematically, this reflects an updated formulation for $\mathbf{G}_o$ and $\mathbf{G}_e$:

$$\mathbf{G}_o = \mathbf{I} \otimes \left(\mathbf{w}_o^\top \mathrm{diag}(\widetilde{\mathbf{x}})\right) \qquad \mathbf{G}_e = \mathbf{I} \otimes \left(\mathbf{w}_e^\top \mathrm{diag}(\widehat{\mathbf{x}})\right), \quad (14)$$

where $\mathbf{w}_o, \mathbf{w}_e \in \mathbb{R}^3$ are weight coefficients for homogenous (x_1^2, x_2^2, x_3^2) and heterogenous ($x_1 x_2$, $x_2 x_3$, $x_1 x_3$) quadratic DOFs. We split $\mathbf{Zz}$ into homogenous and heterogenous parts as $\mathbf{Zz} = \mathbf{G}_o\mathbf{z}_o + \mathbf{G}_e\mathbf{z}_e$. A few manipulations extract the homogenous weight vector as:

$$\begin{aligned}
\mathbf{G}_o\mathbf{z}_o &= \left[\mathbf{I} \otimes (\mathbf{w}_o^\top \mathrm{diag}(\widetilde{\mathbf{x}}))\right]\mathbf{z}_o \\
&= (\mathbf{I} \otimes \widetilde{\mathbf{x}}^\top)(\mathbf{I} \otimes \mathrm{diag}(\mathbf{w}_o))\mathbf{z}_o \\
&= \underbrace{(\mathbf{I} \otimes \widetilde{\mathbf{x}}^\top)\left[\mathrm{diag}(\mathbf{q}_{o_1})|\mathrm{diag}(\mathbf{q}_{o_2})|\mathrm{diag}(\mathbf{q}_{o_3})\right]^\top}_{\mathbf{W}_o}\mathbf{w}_o.
\end{aligned} \quad (15)$$

Together with $\mathbf{W}_e = (\mathbf{I} \otimes \widehat{\mathbf{x}}^\top)\left[\mathrm{diag}(\mathbf{q}_{e_1})|\mathrm{diag}(\mathbf{q}_{e_2})|\mathrm{diag}(\mathbf{q}_{e_3})\right]^\top$, we construct the matrix $\mathbf{W} = [\mathbf{W}_o|\mathbf{W}_e]$ such that $\mathbf{Zz} = \mathbf{Ww}$, where $\mathbf{w} = [\mathbf{w}_o^\top, \mathbf{w}_e^\top]^\top$ is the quadratic weight vector. Clearly, both $\mathbf{z}$ and $\mathbf{w}$ are unknown and final weight coefficients should be calculated alternatingly. We initialize $\mathbf{w}$ as the principal weight, fix it, and compute the current optimal $\mathbf{z}$ using least square as: $\mathbf{z} \leftarrow (\mathbf{Z}^\top\mathbf{Z})^{-1}\mathbf{Z}^\top\Delta\mathbf{u}_k$. Afterwards, $\mathbf{z}$ is fixed, and we compute the optimal $\mathbf{w}$ respecting the updated $\mathbf{z}$. The iteration stops when $\|\Delta\mathbf{u}_k - \mathbf{Ww}\|$ converges.

To avoid irregular weight distributions, we also added a penalty term when solving $\mathbf{w}$. Let $\mathbf{L} \in \mathbb{R}^{6N \times 6N}$ be a graph-Laplacian matrix computing the weight difference between a node and its local average. The augmented optimization for $\mathbf{w}$ becomes:

$$\arg\min_{\mathbf{w}} \|\Delta\mathbf{u}_k - \mathbf{Ww}\| + \alpha\|\mathbf{Lw}\|, \qquad (16)$$

which leads to the final weight update as $\mathbf{w} \leftarrow (\alpha\mathbf{L}^\top\mathbf{L} + \mathbf{W}^\top\mathbf{W})^{-1}\mathbf{W}^\top\Delta\mathbf{u}_k$. Here, we set $\alpha = 0.1$ in all of our experiments. $\alpha\mathbf{L}^\top\mathbf{L} + \mathbf{W}^\top\mathbf{W} \in \mathbb{R}^{6N \times 6N}$ is a big matrix and explicitly factorizing it is expensive. Fortunately, it is also block dominant since $\mathbf{W}^\top\mathbf{W}$ is block diagonal. As a result, we use the iterative block-Jacobi solver to solve $\mathbf{w}$ efficiently. For instance for the bunny model, block-Jacobi can complete one weight update within tens of milliseconds while the Pardiso solver takes several seconds. As shown on the left, few (3 to 5 iterations) alternations are sufficient to produce good quadratic weights.
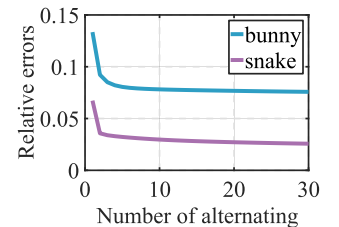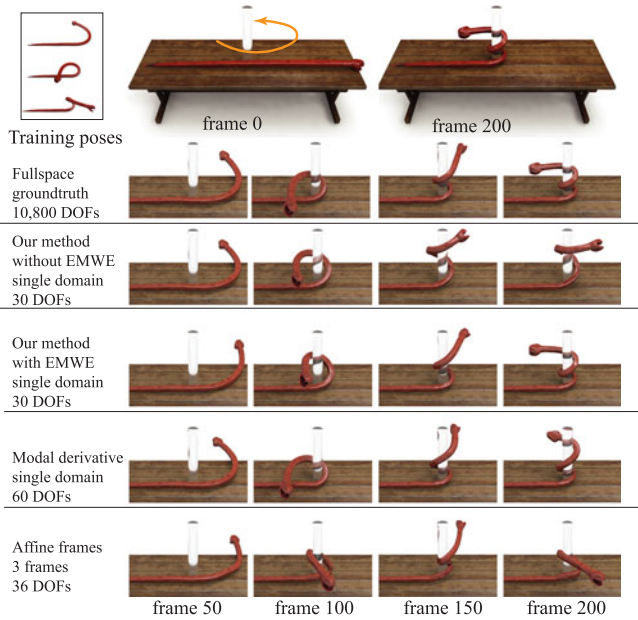
Fig. 8. Comparative simulation of a winding snake.

EMWE enriches the expressivity of the geometric displacement matrix and allows interesting deformable effects that could be challenging for exiting methods with similar numbers of simulation DOFs. Fig. 8 reports snapshots from a set of comparative simulations of a winding snake model. A circular force field is applied and the fullspace simulation with 10,800 DOFs winds the snake for about $800°$ (i.e., $360° + 360° + 180°$) as shown in the first row in the figure. Applying the principal weight for all the 30 DOFs only yields a 360-degree wind (second row in the figure). This result is similar to what one could obtain using *modal derivatives* [4] with 30 modal bases. However, EMWE using only three poses is able to improve the resulting animation making it visually similar to the fullspace result (third row in the figure). This result is even more plausible than modal derivatives with 60 bases (forth row in the figure). Notice that training poses used are quite different from the final frame of the fullspace simulation. Indeed, these poses simply imply that larger weights should be assigned to quadratic DOFs at the middle part of the snake. The entire EMWE training takes less than 300 ms. Results using multiple domains but with only affine transformations as in [10] are also reported in the bottom row. Clearly our method outperforms the spatial reduction using linear DOFs.

6 ADAPTABILITY AND EXTENSIBILITY

Assembling **G** only needs to solve domain's rest-shape stiffness matrix (i.e., for handling Eq. (10) and computing the principal weight), which is efficient and allows an interactive DOF adaption during the simulation runtime to incorporate novel deformations, for example induced by collisions. Besides, the locality of domain's subspace also makes the Cubature training orders of magnitude faster and parallelizable at each Voronoi segment. Overlapping domains do not need an explicit domain coupling treatment. Therefore, our method is able to simulate extreme-scale deformations robustly even when the mesh geometry is degenerated.

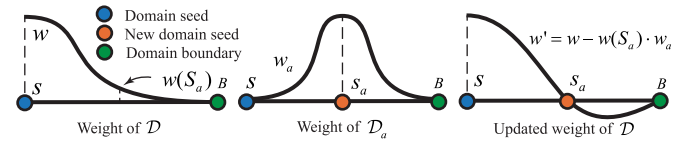*Runtime domain adaption*. It is known that geometrically constructed shape functions can be conveniently altered

Fig. 9. Left: the initial weight distribution w of an existing domain seeded at S. Mid: the weighting function of a newly inserted domain w_a. Right: the updated weighting function w' can be fast obtained as the linear combination of w and w_a.

and adapted at the run time to accommodate new deformations [10], [45]. Our elastic weighting function also possesses this property. Suppose a novel deformation is triggered by a local contact on the deformable body. A reasonable reaction is to add a new domain $\mathcal{D}_a$ seeded at the node where the deepest inter-penetration is found. Due to the presence of $\mathcal{D}_a$, weight functions of existing domains that overlap with $\mathcal{D}_a$ need to be updated.

Consider a 1D example shown in Fig. 9. The original weight function of an existing domain $\mathcal{D}$ seeded at S, as well as the newly-plugged domains $\mathcal{D}_a$ seeded at S_a are known. The weight interpolating property requires that the updated weight w' of $\mathcal{D}$ must have vanished values at both B (the original domain boundary) and S_a while remaining 1 at its own seed S. In other words, we seek for a smooth function to offset w such that it becomes 0 at S_a while its original values at S and B are unchanged. Interestingly, w_a serves this purpose perfectly as it evaluates 0 at both S and B so that stacking w_a over w will not change w's original boundary conditions. As a result, the updated weight function of $\mathcal{D}$, after $\mathcal{D}_a$ is inserted, can be instantly obtained without resorting to the re-computation from scratch as

$$w' = w - w(S_a) \cdot w_a. \tag{17}$$

It is noteworthy that such combination of weight functions also agrees with the superposition principle of linear elasticity. If principal directions of $\mathcal{D}$ and $\mathcal{D}_a$ align each other, it can be shown that the updated weight distribution w' is identical to the fresh-calculated elastic weight, under new boundary conditions. Eq. (17) also implies that the new weight from $\mathcal{D}_a$ *supplements* existing subspaces rather than *replacing* them. In the example shown in Fig. 10, a concentrated external force is applied at the facet center of a rubber brick. Inserting a new domain correspondingly yields a natural denting effect. The updated weight functions on the surface are also plotted.

Parallelized local Cubature. An efficient integration to compute the reduced internal force and its gradient is important for interactive deformable models. Barbič and James [4] found that entries of $\tilde{\mathbf{f}}$ and $\tilde{\mathbf{K}}$ are low-degree polynomials of the reduced displacement for StVK materials, whose
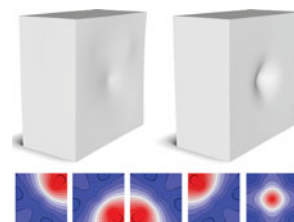

Fig. 10. Adding new domain produces natural denting effects on the brick.

Fig. 11. Use reduced IFE simulation to imitate the inflation of a hot-air balloon. In this example, we simply use Cubature points as restorative elements. Three domains are defined.

TABLE 1
Model Statistics and Simulation Benchmarks

Model	#Ele	#D	#Cub	Pre	Sim	FPS
Bunny	64 K	5	389	2 (4.2%)	26	16
Balloon	56 K	3	248	1 (3%)	55	25
Stay-Puft	49 K	5	138	0.5 (5%)	23	13
Cactus	23 K	4	102	0.2 (4.5%)	175	63
Armadillo	39 K	6	348	1.5 (7%)	31	23

#Ele: the number of elements on the simulation mesh; **#D**: the number of initialized quadratic domains; **#Cub**: the number of cubature elements in total; **Pre**: pre-computation time in minutes (with multi-threading enabled) and the accuracy of the Cubature training; **Sim**: average FPS for simulating the deformable bodies (collision handling not included). **FPS**: over all FPS including collision/self-collision handling and OpenGL rendering.

coefficients can be pre-computed. Another more general solution named Cubature [44] uses 3D quadrature to approximate the internal force at a few Cubature elements. Cubature was originally adopted for model reduction using global bases, and we notice that this procedure can be significantly accelerated under our framework due to the locality of the per-domain subspace.

It is clear that (i.e., in Fig. 4) elements in the same Voronoi segment are affected by the same subset of reduced DOFs from adjacent domains. As a result, the Cubature training can be carried out segment by segment. Such local training is independent and can be trivially accelerated with multi-threading. More importantly because a segment has much fewer (typically less than 20) Cubature points, the associated NNLS (non-negative least square) solves run much faster than the global Cubature training. For instance, training the bunny model would take more than three hours with global bases, which is only less than two minutes when domain-decomposed. After the Cubature training is finished, the runtime evaluation of force and force gradient is simplified as: $\widetilde{\mathbf{f}}_{int} \approx \sum_l \eta_l \mathbf{P}_l \frac{\partial \mathbf{F}_l}{\partial \mathbf{q}}$ and $\widetilde{\mathbf{K}} \approx \sum_l \eta_l (\frac{\partial \mathbf{F}_l}{\partial \mathbf{q}})^\top (\frac{\partial \mathbf{P}_l}{\partial \mathbf{F}_l})^\top \frac{\partial \mathbf{F}_l}{\partial \mathbf{q}}$, where η_l is the non-negative Cubature weight at the element l.

Recovering domain degeneration. Some materials such as the StVK model suffer the stability issue under a large compression. This is because the constitutive law does not produce necessary resisting forces to restore the volume from degeneration. This issue is often invisible for spectral reduction methods as the high-frequency displacements are already filtered by the subspace. Unfortunately, we do not have any mechanism preventing a domain from inversion. To deal with the domain degeneration, we transplant the invertible finite element or IFE method [40], [46] into our framework. IFE alters singular values of $\mathbf{F}$ if they are smaller than a certain threshold so that an element always produces restoring internal forces. Doing so modifies the differential relation between PK1 and the deformation gradient. We follow the formulation in [47] to update $\partial \mathbf{P}/\partial \mathbf{F}$. While $\mathbf{F}$ is linearly related to the reduced coordinate, clamping its singular values does not alter this relation. Therefore, $\partial \mathbf{F}/\partial \mathbf{q}$ remains unchanged.

In general, IFE is slow because the deformation gradient at each element must be checked and adjusted if necessary. This leads to $O(N)$ runtime efforts, and an interactive IFE simulation is hardly possible for large meshes, where N stands for the total number of elements on the mesh. We note that such calculation could also be accelerated following the idea of numerical quadrature, which has also been successfully utilized to resolve self-contacts [48] recently. We follow the standard Cubature procedure to find a small

number of *restorative elements* $\mathcal{R}$ so that the domain-wise restoring force can be well approximated at restorative elements based on a set of degenerated training poses. The runtime corrective forces resolving the volume inversion can then be computed via

$$\widetilde{\mathbf{f}}_r = \sum_{i \in \mathcal{R}} \upsilon_i \mathbf{G}_i^\top \left[\mathbf{f}_i(\widehat{\mathbf{F}}_i) - \mathbf{f}_i(\mathbf{F}_i) \right], \tag{18}$$

where $\mathbf{f}(\mathbf{F}_i)$ and $\mathbf{f}(\widehat{\mathbf{F}}_i)$ are element internal forces calculated using the current deformation gradient $\mathbf{F}_i$ and the singular-value-corrected deformation gradient $\widehat{\mathbf{F}}_i$. υ_i is the non-negative weight. The approximation of Eq. (18) does not have to be precise, because the restoring force itself is ad-hoc when a material failure occurs. $\mathbf{f}_r$ only provides a momentum to recover the degenerated volume, and it will be replaced by regular Cubature forces as long as the degeneration is resolved. In practice, the reduced IFE produces physically-plausible responses under extreme deformations and it is at least an order faster than the fullspace IFE method. Fig. 11 shows an example of using our reduced IFE to imitate inflating a collapsed hot-air balloon.

7 EXPERIMENTAL RESULTS

Our system was implemented using `Microsoft Visual Studio 2013` on a `Windows 10 X64` desktop PC equipped with an `Intel Core i7-5960` CPU and 12 G RAM. Numerical algorithms were implemented on the top of `Eigen C++` template and `Intel MKL` library. Unless specified, the performance reported is with the single-core implementation. The statistics of tested 3D models and simulation benchmarks are summarized in Table 1. Since our method uses the model reduction, all the experiments run at an interactive rate, which is two to three orders faster than the fullspace simulation. Here we would like to remind readers that the EMWE is only used for funnelling the bunny (Figs. 1 and 16) and winding the snake (Fig. 8) with six and three training poses. All the other experiments discussed are based on the principal weight and local adaption. After all, it is not surprising that EMWE can produce highly stylized animations similar to [49] with carefully selected weight training, which makes the comparison unfair.

Weighting quality. In the first experiment, we compare the proposed elastic weighting with other widely-used weighting algorithms including Harmonics weight [11], radial basis function [35], mean value coordinate [37] and the
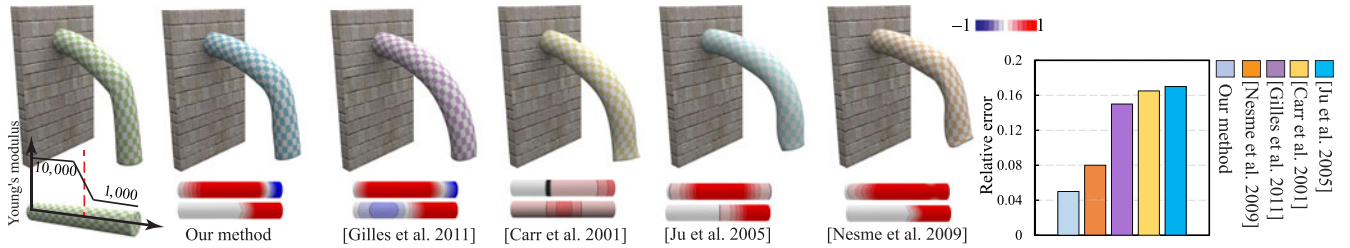
Fig. 12. Compare different weighting algorithms with a cylinder beam of heterogenous materials: the Young's modulus of the beam varies along its neutral axis. Two quadratic domains are set. The weight distributions from different algorithms are also plotted.

method used in [38]. As shown in Fig. 3, quadratic DOFs produce better nonlinear bending than linear or rigid ones. Therefore, we use two quadratic domains (i.e., 60 simulation DOFs) for all the tests in order to eliminate the interference brought by using different simulation DOFs.

The result is summarized in Fig. 12. Here, the material distribution of the cylinder beam is not uniform. The fixed end of the cylinder beam is stiffer where the Young's modulus is set as 10,000. The stiffness linearly decreases to 1,000 at the middle region. The deformed shapes under the gravity are shown along with the corresponding weighting distributions. One can see that geometrically constructed weight functions (Harmonics, RBF and MVC) yield results that do not reflect the material variation. Our method with principal weights well handles such heterogenous elastic object. In [38], the weight function is computed based on a high-resolution equilibrium analysis which also takes the material into account. Similar results can be obtained using *compliance distance* [10], which augments the weight function with Young's modulus. However without computing the principal direction and performing the principal projection, the locking artifact (near the free end of the beam) is discernible. The fullspace ground truth (using un-reduced FEM simulation of linear elements) is the leftmost and the relative error of the free end displacement is also plotted.

One may also notice from Fig. 12 that our weighting function will have negative values occasionally. In fact, in the context of overlapping domain decomposition having negative weighting coefficient is essential to avoid the locking artifact. To explain this argument, let us look at an illustrative toy example of a 1D element with two nodes A and B. Under this configuration, only *interpolation* is needed as shown in the leftmost subfigure of Fig. 13. Here, interpolation means A's weighting function W_A is defined within its nearest boundary condition: $W_A(B) = 0$, and negative weight should be avoided. When a new node C is inserted into this 1D element between A and B,[2] it induces a new boundary condition: $W_A(C) = 0$. That also means W_A need to be *extrapolated* beyond its nearest boundary condition in order to allow A to influence the entire element. If one chooses to design a smooth shape function, in order to incorporate boundary conditions at B and C, the lowest-degree polynomial solution is a quadratic curve with negative values after C (the rightmost subfigure in Fig. 13). If one chooses to clamp the functions values as the bounded biharmonic weights [50], the weighting function becomes discontinuous and locking artifacts could occur (mid sugfigure in Fig. 13). In this case, the element is degenerated to be a linear one. Without

negative weight values, no smooth shape functions can satisfy both boundary conditions at B and C simultaneous.

Whether or not we should have negative weighting functions depends on whether or not the weighting function needs to be extrapolated beyond its nearest boundary conditions. In many existing graphics literature, weighting functions are not supposed to influence areas outside of its neighboring boundary conditions. As a result, such blending is just interpolation and should be convex. However, our system is designed for the overlapping domain decomposition and negative weights become essential. Fig. 14 gives a 3D example. The beam model has two domains both covering the entire model. Their seeds are at the $1/4$ and $3/4$ along the neutral axis of the beam. If BBW is used, weight values of both domains at nodes right to seed 1 will be 1 and 0. This leads to locking effect. However, our method does not have such problem.

Robust nonlinear expressivity. Next, we evaluate the capability of the proposed simulator capturing large nonlinear deformations. We compare our method with two paradigmatic state-of-the-art multi-domain nonlinear simulators using deformation substructuring [1] and coupling elements [2]. As shown in Fig. 15, the cactus model is decomposed into four
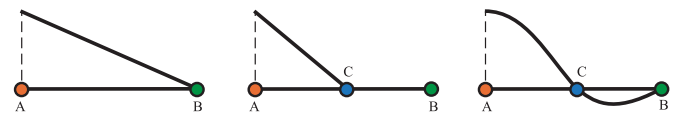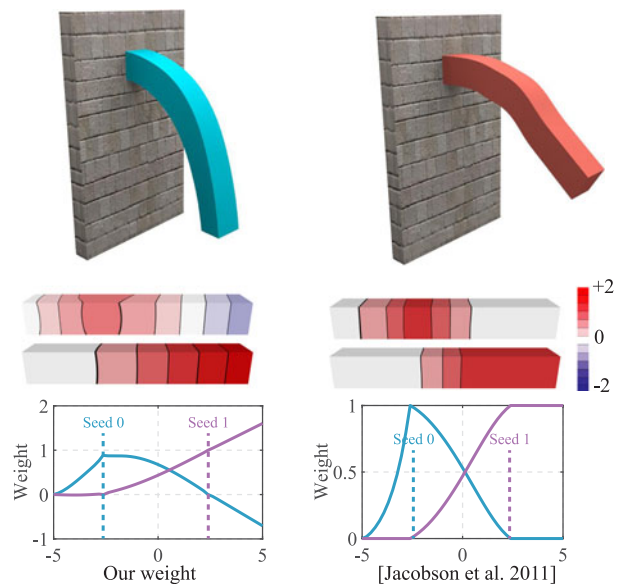

Fig. 13. Shape functions of a simple 1D element.

Fig. 14. BBW may induce locking artifacts.

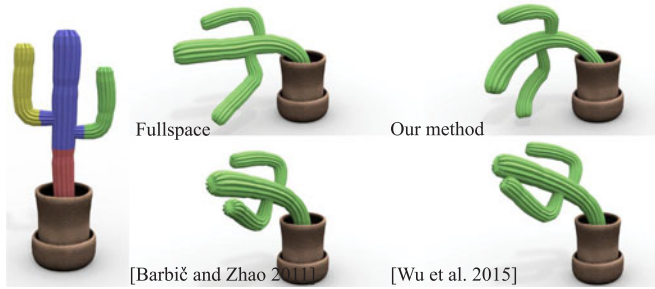2. Doing so actually makes this element nonlinear.

Fig. 15. Simulate a swinging cactus using deformation substructuring [1], unified domain decomposition [2], our method, and the fullspace solver.

domains. The Voronoi segments (left in the figure) are used for the non-overlapping domain decomposition for [1] and [2] with 30 modal derivatives per domain. Therefore all the reduced models have 120 simulation DOFs. From snapshots reported in the figure and the supplementary video, we can see that all the simulators produce plausible deformable animations comparable to the fullspace result.

On the other hand, our method does not require an explicit domain coupling. This advantage makes our system robust against large-scale deformations. Figs. 1 and 16 show snapshots of a challenging scenario: a one-inch-tall bunny model is forced to pass through a thin funnel. The Young's modulus of the bunny is 500 and the Poisson's ratio is 0.4. Five domains are used in this example and all the solvers use 150 simulation DOFs. When the funnel is relatively wide (i.e., 0.4) as shown in Fig. 16 top, all the simulators produce plausible and interesting animations. However, if we reduce the size of the funnel to 0.3, non-overlapping solvers fail. This is because when domains' interfaces are highly distorted, the rigid interface assumption [1] does not hold and the coupling elements [2] are degenerated. Our method
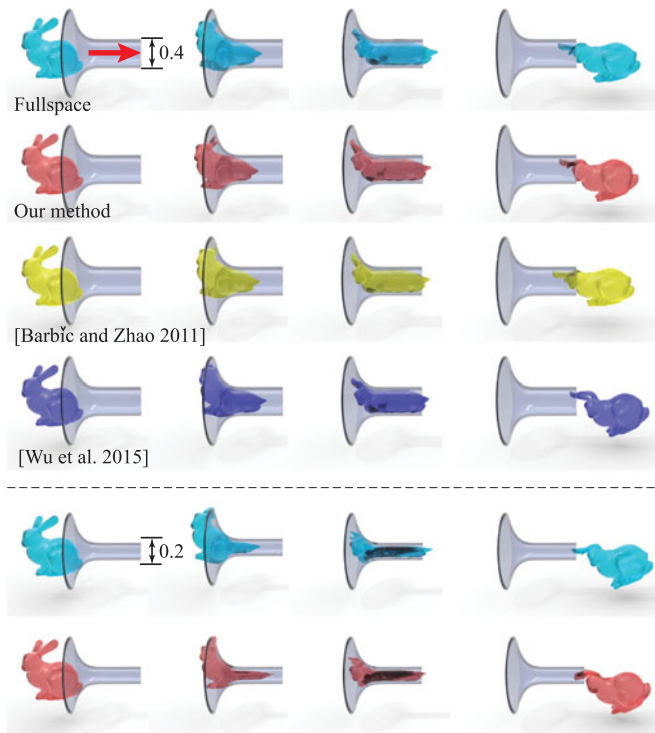

Fig. 16. Drag the bunny through a thin funnel (available as the supplementary executable too).

Fig. 17. Our solver remains stable under severe geometry constraints.

is still able to produce a similar animation compared with the fullspace simulation (Fig. 1) and remains stable even the funnel is further shrunk to 0.2 (Fig. 16 bottom).

A more extreme case highlighting the robustness of our solver is shown in Fig. 17. In this test, we collapse the Armadillo model into a small 2D disk initially. When this strong geometry constraint is released, our method quickly restores the model back to the rest shape with the help of reduced IFE simulation. While the IFE contributes the calculation of necessary internal forces, the main reason behind such good numerical stability is the overlapping domain decomposition. A fullspace IFE [40] simulated animation is also available in the video for readers' reference.

Local adaptivity. Lastly, we test the adaptivity of our algorithm. Fig. 18 reports results using our method, local subspace [28] and the fullspace solver when we push the Stay-Puft with a spiky board. The Stay-Puft model originally has five domains and extra two domains are inserted corresponding to the external collision with spikes. We can see from the figure that, newly-added domains provide necessary deformable freedoms to simulate local deformation, and realistic results comparative to the fullspace ground truth are produced.

It is noteworthy that similar denting effects can also be obtained by building a local subspace using Boussinesq equation [28] as shown in Fig. 18. However, our method is able to deal with a much wider range types of deformation. As shown in Fig. 19, the falling bunny hits an elastic lollipop. The local domain insertion does not only help for a better denting effect on the bunny's body, it also enriches the local deformation for the lollipop. Initially, the bunny has five domains and the lollipop has only one domain seeded at the middle.

8 LIMITATION AND FUTURE WORK

We present a new spatially reduced deformable simulator using overlapping quadratic domains. The incorporated
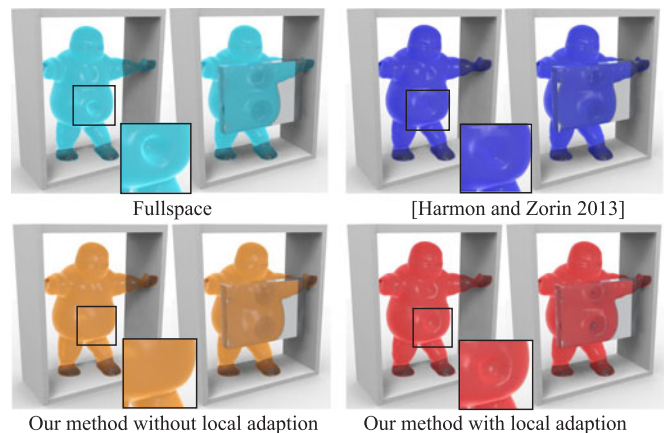

Fig. 18. Adding new domains according to the contacts from a moving spike board greatly enriches detailed local deformation.
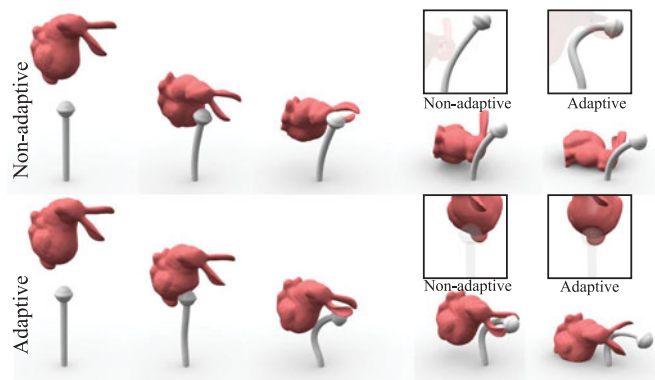
Fig. 19. Runtime domain adaption does not only yield better denting effects on the bunny, but also enriches local deformations at the lollipop.

high-order DOFs enhance the expressivity of the reduced model for nonlinear deformations. Besides, we also design an elastic multi-weight enveloping scheme assigning customized weight functions for quadratic DOFs. Augmented with the accelerated invertible finite element method and runtime domain addition, our method simulates challenging large-scale nonlinear deformations at an interactive rate.

Our method also has several limitations, which leave us many interesting research directions for future work. While quadratic transformations provide plenty of nonlinear freedoms, they could also inject excessive DOFs for modest deformations. As a result, placing a lot of quadratic domains (i.e., over hundreds of domains as in [1]) will quickly drop simulation FPS. A possible solution is to explore the geometric symmetry/degeneration hidden in the deformable body to further condense the domain's DOFs (i.e., downgrade entries in the geometry matrix to linear DOFs that are perpendicular to the neutral axis of a beam, where we have limited nonlinear deformations). Another possible treatment is to use mixed domains, like affine [10] or rigid [11] domains. Adding new domains during the simulation runtime alters the subspace matrix and popping artifacts are possible if the time step size is aggressive. For instance in [28], the time step is set conservatively at the order of $1e^{-4}$ to $1e^{-6}$ to alleviate the issue. Another limitation lies in the fact that our weight function is still computed based on the linear elasticity and the rest shape stiffness matrix. Under large deformations, the weight distribution is likely to change too. We will look into the possibility of calculating the spatial weight derivative similar to the modal derivative [4] to better incorporate such nonlinearity. Augmenting modal deformations with elastic weighting is also an interesting future work for us. In order to do so, we need to carefully design local boundary conditions to construct modal bases and couple them with local rigid body transformations. Of course, doing so will induce more freedoms to the simulator putting us back to the original question for the reduced simulation: how to find the best balance between simulation speed and quality?

ACKNOWLEDGMENTS

REFERENCES

[1] J. Barbič and Y. Zhao, "Real-time large-deformation substructuring," in *Proc. 28th Annu. Conf. Comput. Graph. Interactive Techn.*, 2011, pp. 91:1–91:8.
[2] X. Wu, R. Mukherjee, and H. Wang, "A unified approach for subspace simulation of deformable bodies in multiple domains," *ACM Trans. Graph.*, vol. 34, no. 6, pp. 241:1–241:9, Oct. 2015.
[3] A. Pentland and J. Williams, "Good vibrations: Modal dynamics for graphics and animation," in *Proc. 28th Annu. Conf. Comput. Graph. Interactive Techn.*, 1989, pp. 215–222.
[4] J. Barbič and D. L. James, "Real-time subspace integration for st. venant-kirchhoff deformable models," in *Proc. 28th Annu. Conf. Comput. Graph. Interactive Techn.*, 2005, pp. 982–990.
[5] C. von Tycowicz, C. Schulz, H.-P. Seidel, and K. Hildebrandt, "An efficient construction of reduced deformable objects," *ACM Trans. Graph.*, vol. 32, no. 6, 2013, Art. no. 213.
[6] Y. Yang, D. Li, W. Xu, Y. Tian, and C. Zheng, "Expediting precomputation for reduced deformable simulation," *ACM Trans. Graph.*, vol. 34, no. 6, pp. 243:1–243:13, Oct. 2015.
[7] T. Kim and D. L. James, "Physics-based character skinning using multi-domain subspace deformations," in *Proc. ACM SIGGRAPH/ Eurographics Symp. Comput. Animation*, 2011, pp. 63–72.
[8] F. G. García, T. Paradinas, N. Coll, and G. Patow, "Cages: A multilevel, multi-cage-based system for mesh deformation," *ACM Trans. Graph.*, vol. 32, no. 3, pp. 24:1–24:13, Jul. 2013.
[9] T. W. Sederberg and S. R. Parry, "Free-form deformation of solid geometric models," in *Proc. 13th Annu. Conf. Comput. Graph. Interactive Techn.*, 1986, pp. 151–160.
[10] F. Faure, B. Gilles, G. Bousquet, and D. K. Pai, "Sparse meshless models of complex deformable solids," in *Proc. 28th Annu. Conf. Comput. Graph. Interactive Techn.*, 2011, pp. 73:1–73:10.
[11] B. Gilles, G. Bousquet, F. Faure, and D. K. Pai, "Frame-based elastic models," *ACM Trans. Graph.*, vol. 30, no. 2, pp. 15:1–15:12, Apr. 2011.
[12] S. Martin, P. Kaufmann, M. Botsch, E. Grinspun, and M. Gross, "Unified simulation of elastic rods, shells, and solids," *ACM Trans. Graph.*, vol. 29, no. 4, pp. 39:1–39:10, Jul. 2010.
[13] S. Capell, S. Green, B. Curless, T. Duchamp, and Z. Popović, "A multiresolution framework for dynamic deformations," in *Proc. ACM SIGGRAPH/Eurographics Symp. Comput. Animation*, 2002, pp. 41–47.
[14] E. Grinspun, P. Krysl, and P. Schröder, "Charms: A simple framework for adaptive simulation," in *Proc. 29th Annu. Conf. Comput. Graph. Interactive Techn.*, 2002, pp. 281–290.
[15] X. C. Wang and C. Phillips, "Multi-weight enveloping: Least-squares approximation techniques for skin animation," in *Proc. ACM SIGGRAPH/Eurographics Symp. Comput. Animation*, 2002, pp. 129–138.
[16] A. Nealen, M. Müller, R. Keiser, E. Boxerman, and M. Carlson, "Physically based deformable models in computer graphics," in *Comput. Graph. Forum*, vol. 25, no. 4, 2006, pp. 809–836.
[17] E. Sifakis and J. Barbic, "Fem simulation of 3D deformable solids: A practitioner's guide to theory, discretization and model reduction," in *Proc. 28th Annu. Conf. Comput. Graph. Interactive Techn.*, 2012, pp. 20:1–20:50.
[18] Y. Zhu, E. Sifakis, J. Teran, and A. Brandt, "An efficient multigrid method for the simulation of high-resolution elastic solids," *ACM Trans. Graph.*, vol. 29, no. 2, pp. 16:1–16:18, Apr. 2010.
[19] R. Tamstorf, T. Jones, and S. F. McCormick, "Smoothed aggregation multigrid for cloth simulation," *ACM Trans. Graph.*, vol. 34, no. 6, pp. 245:1–245:13, Oct. 2015. [Online]. Available: http://doi.acm.org/10.1145/2816795.2818081
[20] F. Hecht, Y. J. Lee, J. R. Shewchuk, and J. F. O'Brien, "Updated sparse cholesky factors for corotational elastodynamics," *ACM Trans. Graph.*, vol. 31, no. 5, pp. 123:1–13, Oct. 2012.
[21] M. Fratarcangeli, V. Tibaldo, and F. Pellacini, "Vivace: A practical gauss-seidel method for stable soft body dynamics," *ACM Trans. Graph.*, vol. 35, no. 6, 2016, Art. no. 214.
[22] H. Wang and Y. Yang, "Descent methods for elastic body simulation on the GPU," *ACM Trans. Graph.*, vol. 35, no. 6, 2016, Art. no. 212.

[23] K. K. Hauser, C. Shen, and J. F. O'Brien, "Interactive deformation using modal analysis with constraints," in *Graphics Interface*. San Rafael, CA, USA: Morgan & Claypool, Jun. 2003, pp. 247–256.

[24] M. G. Choi and H.-S. Ko, "Modal warping: Real-time simulation of large rotational deformation and manipulation," *IEEE Trans. Vis. Comput. Graph.*, vol. 11, no. 1, pp. 91–101, Jan. 2005.

[25] T. Kim and D. L. James, "Skipping steps in deformable simulation with online model reduction," *ACM Trans. Graph.*, vol. 28, no. 5, pp. 123:1–123:9, Dec. 2009.

[26] Y. Yang, W. Xu, X. Guo, K. Zhou, and B. Guo, "Boundary-aware multidomain subspace deformation," *IEEE Trans. Vis. Comput. Graph.*, vol. 19, no. 10, pp. 1633–1645, Oct. 2013.

[27] H. Xu and J. Barbič, "Pose-space subspace dynamics," *ACM Trans. Graph.*, vol. 35, no. 4, 2016, Art. no. 35.

[28] D. Harmon and D. Zorin, "Subspace integration with local deformations," *ACM Trans. Graph.*, vol. 32, no. 4, pp. 107:1–107:10, Jul. 2013.

[29] Y. Teng, M. Meyer, T. DeRose, and T. Kim, "Subspace condensation: Full space adaptivity for subspace deformations," *ACM Trans. Graph.*, vol. 34, no. 4, pp. 76:1–76:9, Jul. 2015.

[30] J. Mezger, B. Thomaszewski, S. Pabst, and W. Straber, "Interactive physically-based shape editing," *Comput. Aided Geometric Des.*, vol. 26, no. 6, pp. 680–694, 2009.

[31] A. W. Bargteil and E. Cohen, "Animation of deformable bodies with quadratic bÉzier finite elements," *ACM Trans. Graph.*, vol. 33, no. 3, pp. 27:1–27:10, Jun. 2014.

[32] M. Müller, B. Heidelberger, M. Teschner, and M. Gross, "Meshless deformations based on shape matching," *ACM Trans. Graph.*, vol. 24, no. 3, pp. 471–478, 2005.

[33] A. Jacobson, Z. Deng, L. Kavan, and J. P. Lewis, "Skinning: Real-time shape deformation (full text not available)," in *Proc. ACM 28th Annu. Conf. Comput. Graph. Interactive Techn.*, 2014, pp. 24:1–24:1.

[34] P. Joshi, M. Meyer, T. DeRose, B. Green, and T. Sanocki, "Harmonic coordinates for character articulation," *ACM Trans. Graph.*, vol. 26, no. 3, Jul. 2007, Art. no. 71.

[35] J. C. Carr, et al., "Reconstruction and representation of 3D objects with radial basis functions," in *Proc. 28th Annu. Conf. Comput. Graph. Interactive Techn.*, 2001, pp. 67–76.

[36] M. S. Floater, "Mean value coordinates," *Comput. Aided Geom. Des.*, vol. 20, no. 1, pp. 19–27, Mar. 2003.

[37] T. Ju, S. Schaefer, and J. Warren, "Mean value coordinates for closed triangular meshes," *ACM Trans. Graph.*, vol. 24, no. 3, pp. 561–566, Jul. 2005.

[38] M. Nesme, P. G. Kry, L. Jeřábková, and F. Faure, "Preserving topology and elasticity for embedded deformable models," in *Proc. 28th Annu. Conf. Comput. Graph. Interactive Techn.*, 2009, pp. 52:1–52:9.

[39] Y. Wang, A. Jacobson, J. Barbič, and L. Kavan, "Linear subspace design for real-time shape deformation," *ACM Trans. Graph.*, vol. 34, no. 4, 2015, Art. no. 57.

[40] G. Irving, J. Teran, and R. Fedkiw, "Invertible finite elements for robust simulation of large deformation," in *Proc. ACM SIGGRAPH/Eurographics Symp. Comput. Animation*, 2004, pp. 131–140.

[41] A. Shamir, "A survey on mesh segmentation techniques," in *Computer Graphics Forum*. Hoboken, NJ, USA: Wiley Online Library, 2008, vol. 27, no. 6, pp. 1539–1556.

[42] S. Lloyd, "Least squares quantization in PCM," *IEEE Trans. Inf. Theor.*, vol. 28, no. 2, pp. 129–137, Sep. 1982.

[43] S. Boyd and L. Vandenberghe, *Convex Optimization*. Cambridge, U.K.: Cambridge university press, 2004.

[44] S. S. An, T. Kim, and D. L. James, "Optimizing cubature for efficient integration of subspace deformations," in *Proc. 28th Annu. Conf. Comput. Graph. Interactive Techn.*, 2008, pp. 165:1–165:10.

[45] M. Tournier, M. Nesme, F. Faure, and B. Gilles, "Velocity-based adaptivity of deformable models," *Comput. Graph.*, vol. 45, pp. 75–85, 2014.

[46] A. Stomakhin, R. Howes, C. Schroeder, and J. M. Teran, "Energetically consistent invertible elasticity," in *Proc. ACM SIGGRAPH/Eurographics Symp. Comput. Animation*, 2012, pp. 25–32.

[47] F. Sin, Y. Zhu, Y. Li, and D. Schroeder, "Invertible isotropic hyperelasticity using SVD gradients," in *Proc. ACM SIGGRAPH/Eurographics Symp. Comput. Animation*, 2011.

[48] Y. Teng, M. A. Otaduy, and T. Kim, "Simulating articulated subspace self-contact," *ACM Trans. Graph.*, vol. 33, no. 4, pp. 106:1–106:9, Jul. 2014. [Online]. Available: http://doi.acm.org/10.1145/2601097.2601181

[49] S. Martin, B. Thomaszewski, E. Grinspun, and M. Gross, "Example-based elastic materials," *ACM Trans. Graph.*, vol. 30, no. 4, pp. 72:1–72:8, Jul. 2011. [Online]. Available: http://doi.acm.org/10.1145/2010324.1964967

[50] A. Jacobson, I. Baran, J. Popovic, and O. Sorkine, "Bounded biharmonic weights for real-time deformation," *ACM Trans. Graph.*, vol. 30, no. 4, pp. 78–1, 2011.
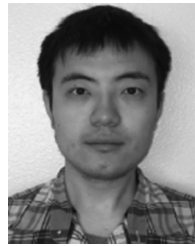
Ran Luo received the bachelor's degree from the Beihang University, previously known as Beijing University of Aeronautics and Astronautics, in 2014. He is currently working toward the PhD degree in computer engineering with the University of New Mexico(UNM), Albuquerque, New Mexico. His research interests include physics-based animation/simulation, virtual reality, machine learning and related topics. He is currently a research assistant in the Department of Electrical and Computer Engineering, University of New Mexico.

Weiwei Xu is a researcher with the State Key Lab of CAD & CG, College of Computer Science, Zhejiang University, awardee of NSFC Excellent Young Scholars Program in 2013. His main research interests include the digital geometry processing, physical simulation and virtual reality. He has published around 60 papers on international graphics journals and conferences, including 16 papers on ACM TOG. He is a member of the IEEE.
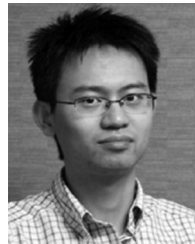
Huamin Wang received the BEng degree from Zhejiang University, the MS degree from Stanford University, and the PhD degree in computer science from the Gerogia Institute of Technology, in 2002, 2004 and 2009. Hw is an associate professor in the Department of Computer Science and Engineering, the Ohio State University. Before joining Ohio State University, he was a postdoctoral researcher in the Department of Electrical Engineering and Computer Sciences, the University of California, Berkeley. He is a member of the IEEE.
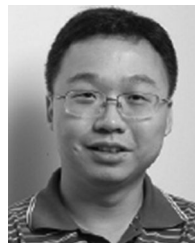
Kun Zhou He received the BS and PhD degrees in computer science from Zhejiang University, in 1997 and 2002, respectively. He is a Cheung Kong professor in the Computer Science Department of Zhejiang University, and the director of the State Key Lab of CAD&CG. Prior to joining Zhejiang University in 2008, he was a leader researcher of the Internet Graphics Group at Microsoft Research Asia. His research interests include the visual computing, parallel computing, human computer interaction, and virtual reality. He currently serves on the editorial/advisory boards of the *ACM Transactions on Graphics* and the *IEEE Spectrum*. He is a fellow of the IEEE.

Yin Yang received the PhD degree in computer science from the University of Texas at Dallas, in 2013. He is an assistant professor in the Department of Electrical Computer Engineering, the University of New Mexico, Albuquerque. His research interests include physics-based animation/simulation and related applications, scientific visualization, and medical imaging analysis. He is a member of the IEEE.

▷ **For more information on this or any other computing topic, please visit our Digital Library at** www.computer.org/publications/dlib.